The Company of Biologists

RESEARCH ARTICLE

Spatial integration of mechanical forces by α-actinin establishes actin network symmetry

Fabrice Senger[1], Amandine Pitaval[1,2], Hajer Ennomani[1], Laetitia Kurzawa[1], Laurent Blanchoin[1,3,*] and Manuel Théry[1,3,*]

ABSTRACT

Cell and tissue morphogenesis depend on the production and spatial organization of tensional forces in the actin cytoskeleton. Actin network architecture is made of distinct modules characterized by specific filament organizations. The assembly of these modules are well described, but their integration in a cellular network is less understood. Here, we investigated the mechanism regulating the interplay between network architecture and the geometry of the extracellular environment of the cell. We found that α-actinin, a filament crosslinker, is essential for network symmetry to be consistent with extracellular microenvironment symmetry. It is required for the interconnection of transverse arcs with radial fibres to ensure an appropriate balance between forces at cell adhesions and across the actin network. Furthermore, this connectivity appeared necessary for the ability of the cell to integrate and to adapt to complex patterns of extracellular cues as they migrate. Our study has unveiled a role of actin filament crosslinking in the spatial integration of mechanical forces that ensures the adaptation of intracellular symmetry axes in accordance with the geometry of extracellular cues.

This article has an associated First Person interview with the first author of the paper.

KEY WORDS: α-Actinin, Cell architecture, Crosslinker, Mechanical force, Symmetry

INTRODUCTION

Actin filaments self-organize into a variety of modules, and the combination of modules can generate a diversity of subcellular architectures (Blanchoin et al., 2014). These modules include lamellipodia, radial fibres, transverse arcs and stress fibres. The lamellipodium consists of branched and entangled filaments. Radial fibres consist of parallel bundles of filaments, which are anchored on focal adhesions and orientated radially towards the cell centre. Transverse arcs and stress fibres are contractile structures consisting of anti-parallel bundles of filaments. Transverse arcs are localized in the lamella and align parallel to adhesive cell edges. Stress fibres connect two distant focal adhesions, and traverse the non-adhesive part of the cell periphery or the central part of the cell (Tojkander et al., 2012).

Actin-based modules are dynamic. In the lamellipodium and radial fibres, actin dynamics is dominated by actin polymerization, whereas in transverse arcs or stress fibre dynamics is governed by acto-myosin contraction. All undergo regulated disassembly. Growth, contraction and disassembly coexist in the cell, leading to complex intracellular patterns of expansion and shrinkage (Levayer and Lecuit, 2012; Belmonte et al., 2017). Furthermore, modules interconvert (Letort et al., 2015). Lamellipodium filaments can align to form transverse arcs when they are pushed away from their site of nucleation at the cell membrane (Burnette et al., 2011; Shemesh et al., 2009). Radial fibres and transverse arcs tend to join and coalesce to form stress fibres (Hotulainen and Lappalainen, 2006; Tojkander et al., 2015). The combination of internal dynamics and interconversion of modules leads to complex dynamic network architectures. Theoretically, this could lead to disordered phases (Mak et al., 2016). However, in cells, it results into surprisingly ordered and reproducible architectures. However, how modules consisting of self-organized filaments of 100 nm to 1 μm in length can result in an architecture that is 10- to 100-fold larger with a geometry and symmetry that is in correspondence with the environment of the cell remains an open question.

Cells respond to a multitude of different chemical and physical signals. This diversity implies a process of integration, which results in a single polarity axis being defined and ensures that this axis is adapted to extracellular cues. For example, epithelial cells assemble specific actin-based architecture at their apical pole and thus orientate their polarity towards the lumen. Migrating cells assemble a characteristic network at the cell front guiding them along signal gradients. This integration process ensures the consistency between intracellular architecture and the geometry of the extracellular environment. The spatial integration of extracellular cues is based on the connectivity of all actin-based modules and the transmission of mechanical forces throughout the entire cell. This transmission acts as a process of integration allowing forces on all adhesion sites to be balanced within a single interconnected architecture. In addition, the contribution of contractile forces to network rearrangement, such as filament displacements and module interconversion, allows the final cell architecture to be geometrically and mechanically consistent with cell microenvironment. Notably, such a remodelling of the actin network by the transmission and balance of contractile forces applied on anchorage sites should allow this network to adopt the same elements of symmetry as the extracellular environment. Here, we interrogate this working model by investigating the architecture and symmetry of contractile actin networks in response to controlled geometrical cues.

RESULTS

Crosslinkers support actin network contraction symmetry *in vitro*

The architecture and polarity of the cellular actin network are shaped by the combined inputs from signalling pathways and structural self-organization. However, the contributions of these respective inputs

[1]Université Grenoble-Alpes, CEA, CNRS, INRA, Interdisciplinary Research Institute of Grenoble, Laboratoire de Physiologie Cellulaire & Végétale, CytoMorphoLab, 3800, Grenoble, France. [2]Université Grenoble-Alpes, CEA, INRA, CNRS, UMR5168, Interdisciplinary Research Institute of Grenoble, Biomics Lab, 38000 Grenoble, France. [3]Université Paris Diderot, INSERM, CEA, Hôpital Saint Louis, Institut Universitaire d'Hematologie, UMRS 1160, CytoMorphoLab, 75010 Paris, France.

*Authors for correspondence (Laurent.blanchoin@cea.fr; Manuel.thery@cea.fr)

M.T., 0000-0002-9968-1779

are difficult, if not impossible, to distinguish. The reconstitution of actin network growth and contraction *in vitro* using purified components is an effective way to investigate network structural self-organization in a system that is independent of the spatial patterning of signalling pathways. Several recent examples illustrate the ability of a reconstituted network to recapitulate key cellular actin network properties, such as anchoring-dependent reinforcement (Ciobanasu et al., 2014), long-range coherence (Ennomani et al., 2016; Linsmeier et al., 2016), contraction-disassembly coupling (Murrell and Gardel, 2012; Reymann et al., 2012; Vogel et al., 2013), symmetry breaking (Abu Shah and Keren, 2014) and scaling of contractile rates (Reymann et al., 2012).

Recently, the spatial distribution of motors was shown to direct the shape changes of contracting actin networks (Schuppler et al., 2016). Interestingly, the asymmetric positioning of anchorage sites generated anisotropic network contraction (Schuppler et al., 2016). However, network deformation is the outcome of the mechanical work of motors on a given network architecture (Reymann et al., 2012). The role of actin network architecture on the direction and symmetry of its contraction remains to be investigated. Here, we addressed this point by looking at the contraction of actin rings *in vitro*.

A given actin network architecture, such as a ring-shaped structure (actin ring), can be created by the surface micropatterning of actin nucleation sites (Reymann et al., 2010), and its contraction can be monitored following the addition of myosin VI, which can bear continuous force without the need to assemble into minifilaments (Fig. 1A,B; Reymann et al., 2012; Ennomani et al., 2016). Surprisingly, with an actin ring, the pattern of contraction was heterogeneous and asymmetric. The initial bias in ring deformation was amplified leading to eccentric contraction. The focus point for the contraction was distant from the centre and nucleation pattern of the initial ring-shaped structure, and therefore appeared not to arise from contraction towards this centre (Fig. 1A,C; Movie 1).

Crosslinkers are key regulators of actin network contractility (Jensen et al., 2015; Ennomani et al., 2016) and are likely to be required for local contraction to be transmitted throughout the network by controlling the network connectivity. Strikingly, the addition of the filament crosslinker, α-actinin (ACTN4), fully restored network contraction symmetry. Actin rings displayed more progressive and regular contraction. The initial ring-shaped structure appeared to be conserved throughout the contractile process, and the final focus point of the contraction was close to the centre of the nucleation pattern (Fig. 1B,D; Movie 1).

α-Actinin knockdown impairs cellular actin network symmetry

These results prompted us to investigate whether actin network crosslinking was required for the transmission of mechanical forces throughout the cell and thereby for the proper integration of extracellular cues during the self-organization of cellular actin network architecture.

Surface micropatterning was used to investigate cell responses to defined adhesion patterns with controlled elements of symmetry and anisotropy (Théry, 2010). On crossbow-shaped patterns, cells developed a stereotypical actin architecture, presenting a branched network forming the lamellipodium along the curved adhesive edge, which further reorganized in the lamella to form radial fibres perpendicular to the curved edge and transverse arcs along the curved edge, as well as an array of ventral stress fibres above non-adhesive edges flanking the central bar of the crossbow pattern (Théry et al., 2006; Schiller et al., 2013; Jiu et al., 2015) (Fig. 2A; Movie 2). α-Actinin localized at focal adhesions, along radial fibres

and transverse arcs, and at the junction between the latter two structures (Fig. 2A; Fig. S1). This localization suggested a potential role in ensuring the connectivity of the entire network and the transmission of contractile forces across the cell body. Indeed high concentrations of α-actinin have been shown to maintain the symmetry of actin network in cells plated on disc-shaped micropatterns, and knockdown of α-actinin reduces the lateral connections of radial fibres, and promoted the symmetry breaking and swirling of actin architectures (Tee et al., 2015).

We attempted to identify the contribution of α-actinin to actin network architecture by downregulating its expression with siRNAs. In non-sarcomeric cells, α-actinin is present in two isoforms, α-actinin-1 (ACTN1) and α-actinin-4 (ACTN4), which play similar but non-redundant role in the regulation of cell motility (Quick and Skalli, 2010). In RPE1 cells, ACTN1 expression level seemed to compensate for ACTN4 downregulation (Fig. S2). Therefore, a double knockdown against both isoforms (denoted siACTN1/4) appeared necessary to efficiently deplete the presence of α-actinins on the network (Fig. S2). The specificity of our siRNA approach was assessed by a redundancy check, that is, the use of a second set of siRNA targeting another sequence of, respectively, ACTN1 and ACTN4 (Fig. S3).

As a result of the double α-actinin knockdown, many cells did not seem to fully spread on the micropatterns. In cells that did spread, the actin network appeared strikingly disorganized (Fig. 2A). It was difficult to decipher whether the remaining fibres were improperly attached transverse arcs or misoriented radial fibres or a mixture of both, as their regular orientation along or normal to the cell edge were strongly perturbed (Fig. 2B). The symmetrical organization of all types of actin bundles appeared to be compromised with respect to the symmetry axis of the fibronectin micropattern (Fig. 2B). Similar disorganizations have been observed previously in U2OS cells, in which the silencing of ACTN1 induced the misorientation and lack of lateral connections of radial fibres which finally disappeared during cell migration (Kovac et al., 2013).

To quantify the structural consequence of α-actinin depletion on the actin network, we first compared the curvature radii of the two peripheral stress fibres. The curvature radii of the two stress fibres on both sides of the micropattern symmetry axis were almost identical in control conditions (with a median ratio of 1.274) and significantly different in α-actinin-depleted cells (with a median ratio of 1.797) (Fig. 2C,D). We then segmented and measured the orientation of actin bundles (Fig. 2E). We compared the cumulative angular distributions away from the axis of micropattern symmetry of individual actin bundles in the two respective halves of the cell on each side of this axis (Fig. 2F,G). In control conditions, the difference in these cumulative angular distributions between the two halves of the cell appeared much lower in the control conditions than after α-actinin depletion, and therefore appeared more in line with the axis of mirror symmetry (Fig. 2F,G). To assess the specificity of α-actinin knockdown in these experiments, we performed rescue experiments, which showed that cells recovered their symmetry upon expression of another α-actinin construct that was not sensitive to the set of siRNAs used (Fig. S4).

α-Actinin knockdown deviates actin flow and nucleus position

By considering that actin bundles result from the conversion of lamellipodium fibres into transverse arcs and further into stress fibres as they move towards the cell centre, it is likely that the misorientated actin bundles in α-actinin-depleted cells were associated with a misorientated inwards flow of contractile transverse arcs. Time-lapse recording of Lifeact–GFP-expressing cells showed that actin bundles assembled near the curved adhesive edge were progressively
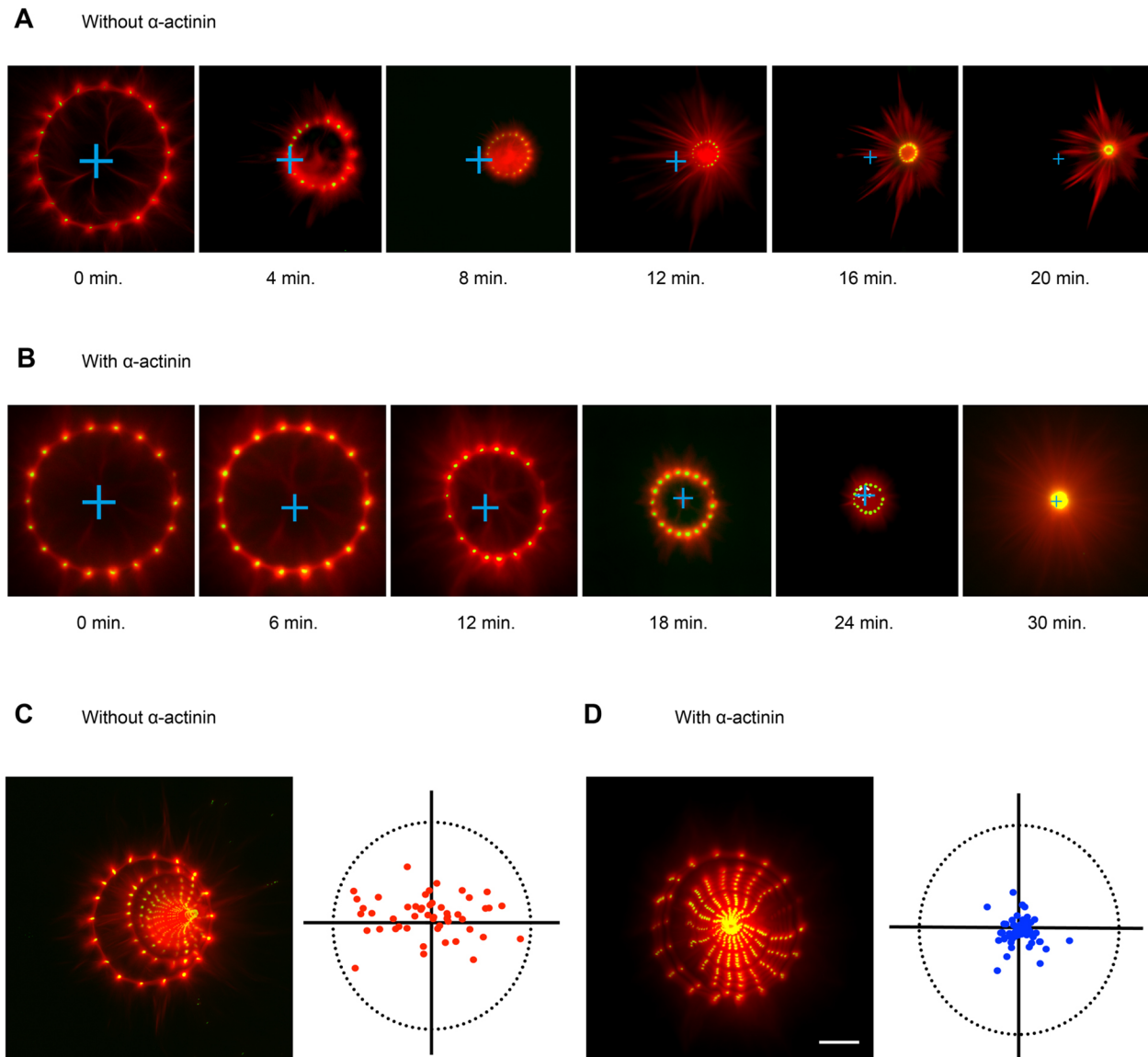
Fig. 1. α-Actinin modulates the symmetry of actin network contractility *in vitro*. Actin ring assembly was initiated from the polymerization of actin filaments from micropatterned dots coated with actin nucleation-promoting factors. (A,B) Contraction of the actin rings upon addition of myosin motors in the absence (A) or presence (B) of α-actinin. Time is indicated in minutes. *t*=0 corresponds to the onset of contraction. The blue cross highlights the geometrical center of the initial actin structure at time, *t*=0. (C,D) Images show the maximum projection of pictures shown in A and B, respectively. The plots represent the coordinates of the centre of the contractile ring after full contraction (C, *n*=73; D, *n*=50). Scale bar: 20 μm.

displaced towards the cell centre over time (Fig. 3A; Movie 3). Image segmentation followed by particle image velocimetry (PIV) was then used to track the moving structures. In control cells, contractile actin bundles converged towards the cell centre, and hence the averaged flow vector was aligned with the micropattern symmetry axis. By contrast, in α-actinin-depleted cells, the average flow vector deviated from the symmetry axis (Fig. 3B,C). These results were consistent with our initial observations of the contraction of acto-myosin rings *in vitro*: both experiments showed that the lack of crosslinker compromised the symmetry of actin network contraction.

The retrograde flow of contractile actin bundles is involved in nucleus positioning (Gomes et al., 2005), as they interact with the nucleus. Asymmetric actin flow could therefore affect the proper positioning of the nucleus. In a control cell, the nucleus was positioned on the symmetry axis, near the cell centre (Fig. 4A,B) whereas in an α-actinin-depleted cell, the nucleus was positioned

away from the cell centre towards one of the two peripheral stress fibres (Fig. 4A,B). Comparison of the distributions of the distance of the nucleus from the symmetry axis confirmed a significant deviation in actinin-depleted cells (Fig. 4C). Hence, these results support the conclusion that α-actinin-mediated regulation of the retrograde flow of contractile actin bundles plays a role in aligning the organization and the symmetry axis of the cell with that of the extracellular environment.

Asymmetric distribution of mechanical forces in α-actinin-depleted cells
We then characterized the molecular machinery and the spatial distribution of mechanical forces associated with cell contractile modules. With respect to the molecular machinery, we examined the localization of non-muscle myosin IIA, IIB and the phosphorylated myosin light chains (pMLC). As expected from previous work
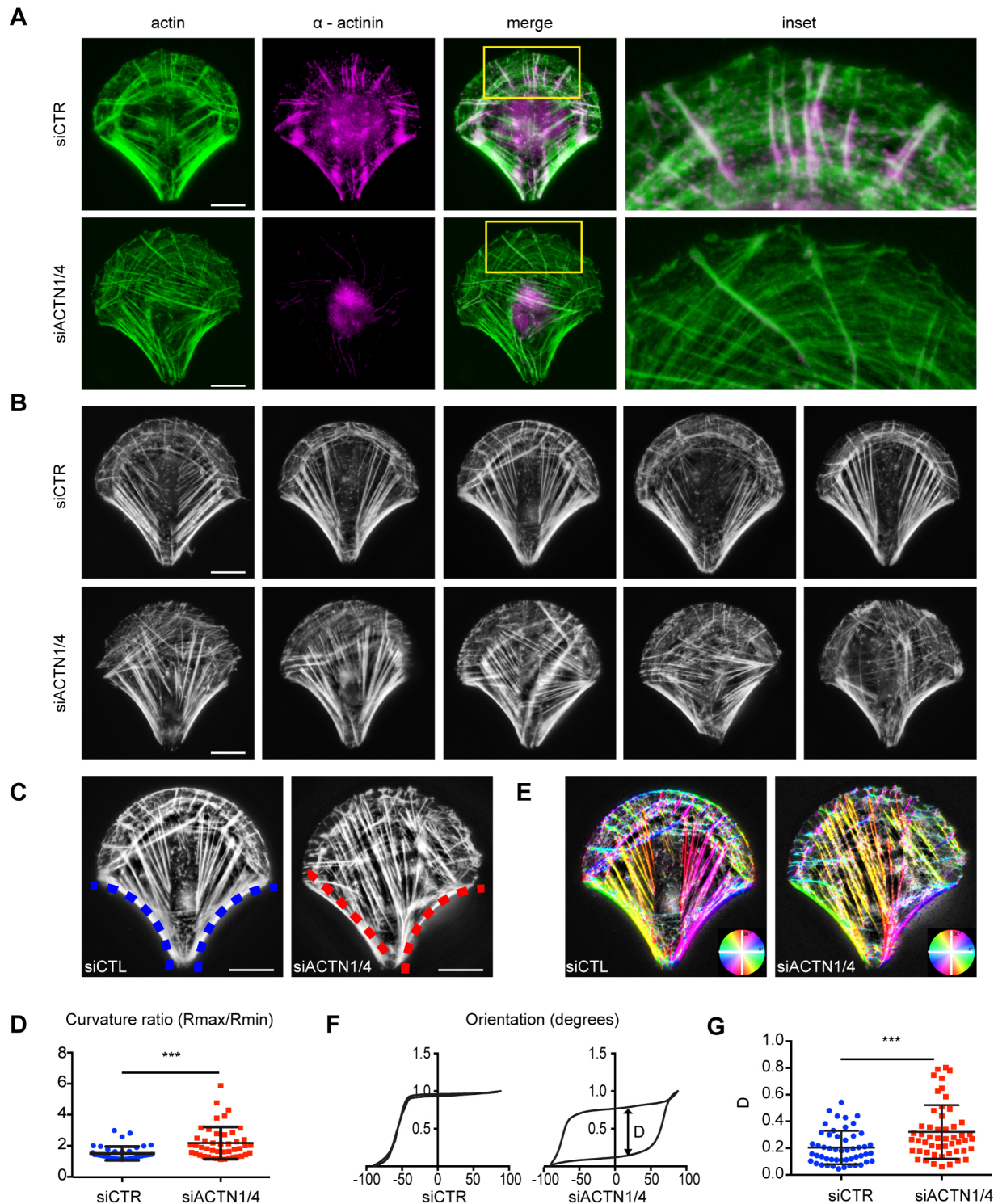
Fig. 2. Reorganization of cellular actin architecture upon α-actinin depletion. (A) RPE1 cells on crossbow-shaped micropatterns were fixed and stained for actin (green) and α-actinin (magenta). Inserts show a magnified view of the upper part of the cell and the loss of α-actinin staining upon α-actinin depletion (siACTN1/4, bottom row). (B) Phalloidin staining revealing F-actin architecture in control (siCTR) and α-actinin-depleted cells (siACTN1/4). (C) Measurement of the curvature of the two non-adherent edges in control (siCTR, blue dashed lines) and α-actinin-depleted cells (siACTN1/4, red dashed lines). (D) The maximal curvature (Rmax) to minimal curvature (Rmin) ratio was calculated and plotted for the control (*n*=43) and α-actinin-depleted cells (*n*=45). (E) Detection and measurement of internal actin bundle orientation. Actin fibre orientation is colour coded according to the colour-wheel inset. (F) Examples of cumulative distribution of actin bundle angles as determined by orientation analysis for control and α-actinin-depleted cells. In each graph, the two curves correspond to angular distributions of the left and the right half of the cell with respect to the micropattern symmetry axis. The two curves were compared by measuring their maximal difference, D. (G) Plot showing the values of parameter D for control (*n*=51) and α-actinin-depleted cells (*n*=52). Images have been background subtracted and contrast enhanced as described in the Materials and Methods. ***P<0.001 (Mann–Whitney test). Scale bars: 10 µm.
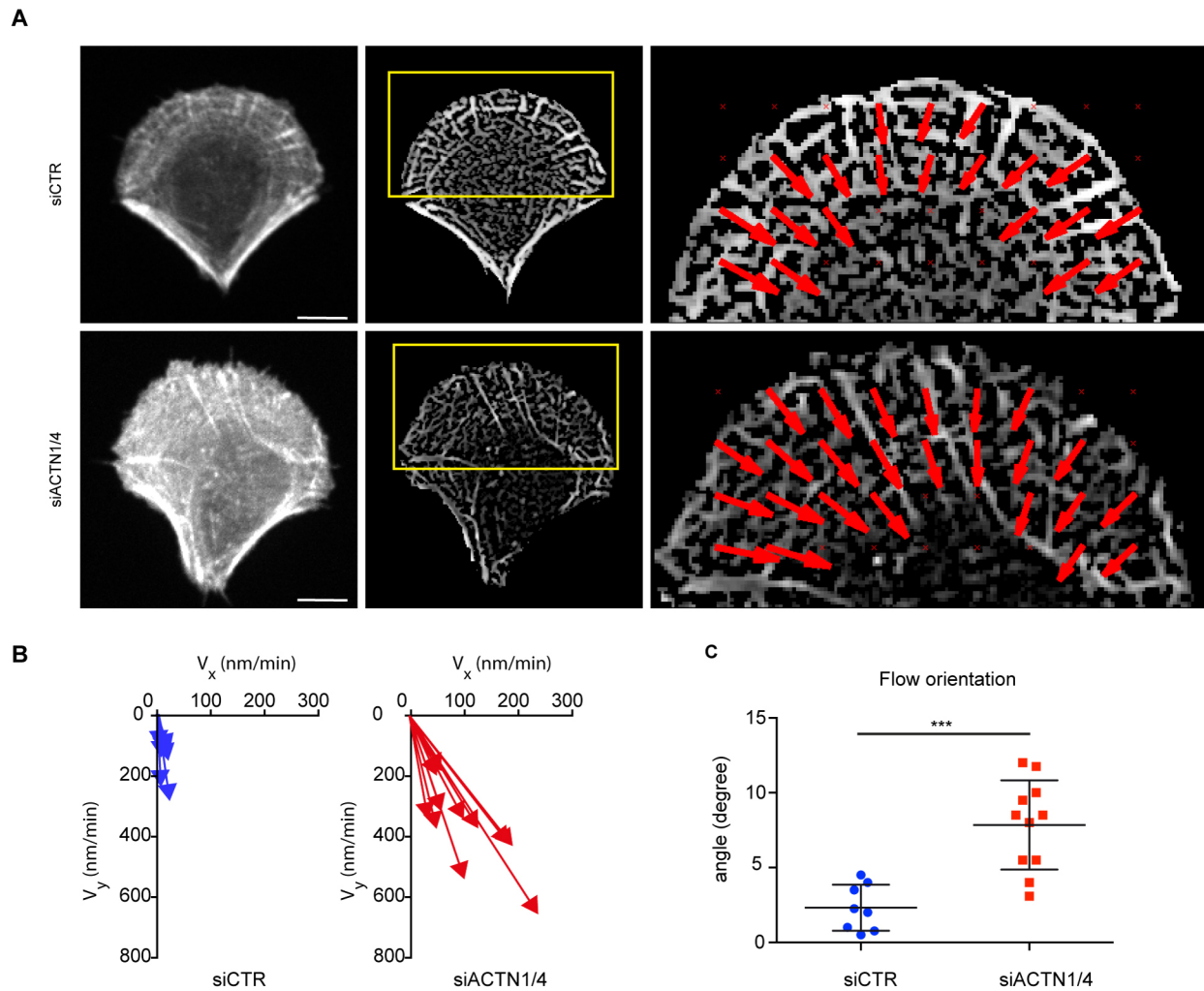
Fig. 3. Effect of α-actinin depletion on retrograde actin network flow. (A) Images show the LifeAct–GFP signal in live RPE1 cells plated on crossbow-shaped micropatterns (left), filtered images with noise removed (centre) and a zoomed image of the PIV flow on the upper part of the cell (right). Red arrows show the flow orientation. (B) Graphs show the orientations of the averaged flow in different cells. Arrow lengths correspond to the averaged flow speed, and Vx and Vy to their Cartesian coordinates. (C) Plots show the value of the angular deviation of the average flow with respect to the micropattern symmetry axis for control (n=8) and α-actinin-depleted cells (n=11). ***P=0.0003 (Mann–Whitney test). Scale bars: 10 μm.

(Naumanen et al., 2008), these myosin components were found on transverse arcs and stress fibres (Fig. 5A). In accordance with the alignment of the actin modules with the axis of symmetry of the crossbow micropattern, the distributions of myosin components appeared precisely symmetrical with respect to this axis in control cells but significantly biased in α-actinin-depleted cells (Fig. 5B). The myosin-component asymmetry stemmed from the asymmetry of the two peripheral stress fibres as well as from defective transverse arcs. These transverse arcs were less bundled and were misorientated compared with those in control cells, in which they formed conspicuous and regular circular arcs lining the curved cell edge.

The contractile forces produced by these myosins also appeared asymmetrically distributed in α-actinin-depleted cells. To measure these forces, we used fibronectin micropatterns on polyacrylamide hydrogels in which fiduciary beads were embedded (Vignaud et al., 2014). Cells were first plated onto those micropatterns and then detached. The bead displacement field associated with hydrogel relaxation following cell detachment was monitored and computed to infer the associated traction force field (Martiel et al., 2015).

As expected (Tseng et al., 2011; Schiller et al., 2013; Sun et al., 2016), forces were evenly distributed along the curved adhesive edge,

and were similarly concentrated at each extremity of the edge, and at the extremity of the central bar corresponding to the apex of the fan shaped distribution of contractile bundles (Fig. 5C). In α-actinin-depleted cells, the forces were less evenly distributed along the curved adhesive edge, and tended to be concentrated at only one of the two extremities of the edge (Fig. 5C). The lower concentration of forces at the extremity of the edge was consistent with the defective assembly of transverse arcs and the misorientation of stress fibres. The main orientation of the traction force field was then characterized by measuring the first-order moment of the force vector field (Butler et al., 2002; Mandal et al., 2014). In control cells, the traction force field was generally aligned with the micropattern symmetry axis (Fig. 5C,D). By contrast, in α-actinin-depleted cells, it often appeared to be deflected from the symmetry axis, reflecting the greater concentration of traction forces at only one of the two extremities of the curved adhesive edge (Fig. 5C,D). Nevertheless, α-actinin-depleted cells were able to produce traction forces that were even stronger than the forces produced in control cells, as previously reported (Oakes et al., 2012; Roca-Cusachs et al., 2013). Some of the forces were aligned with the symmetry axis and appeared to be produced above non-adhesive regions by central or peripheral stress
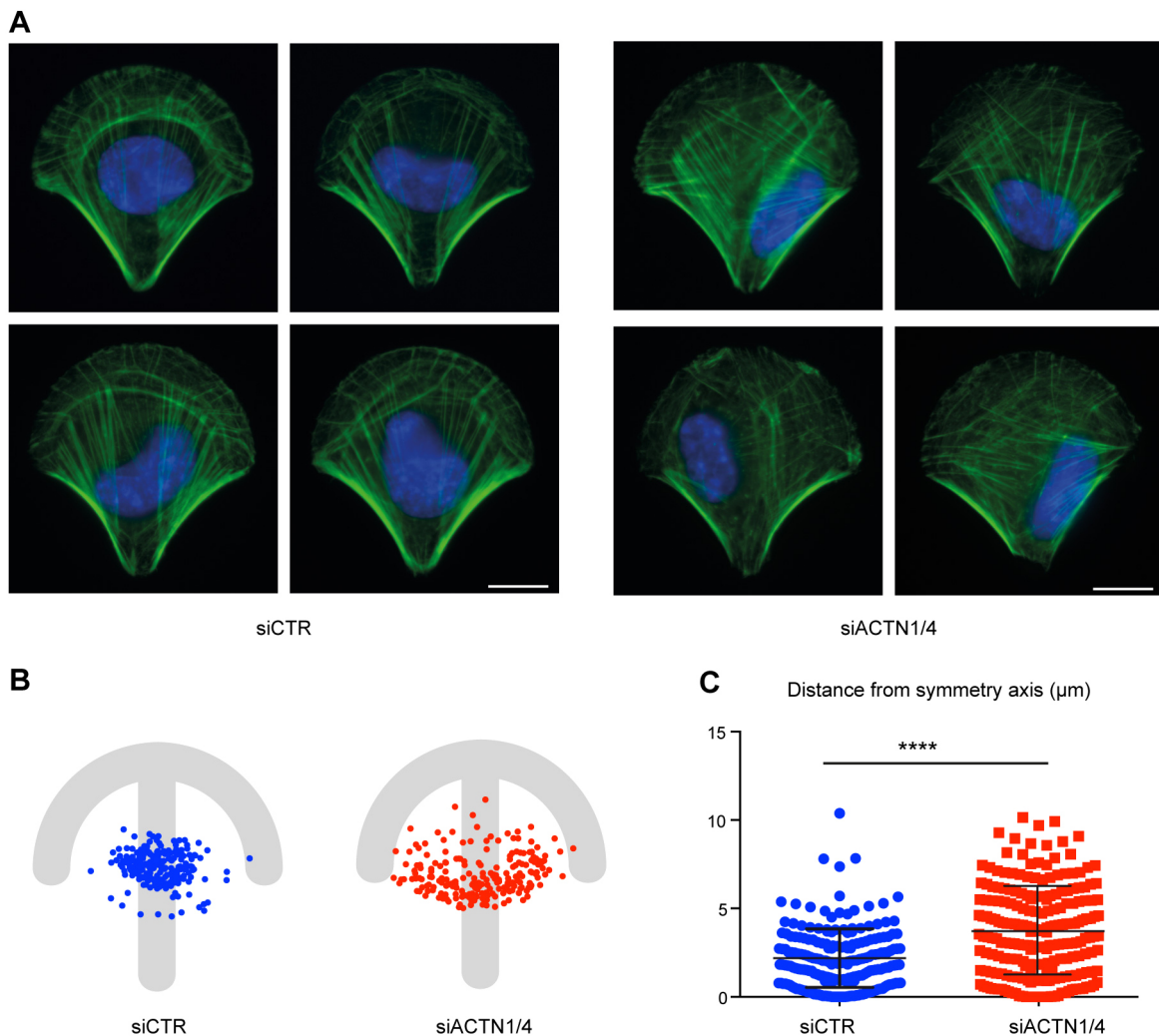
Fig. 4. Mispositioning of the nucleus upon α-actinin depletion. (A) F-actin (green) and nuclei (DAPI, blue) staining in control (siCTR) and α-actinin (siACTN1/4)-depleted cells. (B) Spatial distribution of positions of centres of mass of nuclei in control (siCTR, blue, *n*=210) and depleted cells (siACTN1/4, red, *n*=214) with respect to the micropattern. (C) The plot shows the distance between the centre of mass of the nucleus and the symmetry axis of the micropattern in control (siCTR, blue, *n*=210) and α-actinin-depleted cells (siACTN1/4, red, *n*=214). ****$P<0.0001$ (Mann–Whitney test). Scale bars: 10 µm.

fibres. Therefore, the forces driving the asymmetry in the traction force field may have been due to the forces produced in the lamella by the misorientated transverse arcs that were positioned at the curved adhesive edge and across the symmetry axis.

Defective force transmission across the cell in α-actinin-depleted cells

To characterize force transmission along the curved adhesive edge and perpendicular to the symmetry axis, we looked more closely at the network architecture by analysing the actin network skeleton and by measuring forces relaxation in response to nano-ablation of subcellular structures.

The integrity of network architecture in the lamella relies on the connection of radial fibres with transverse arcs and on the redistribution of contractile forces produced in the arcs toward adhesion sites via radial fibres. The structural integrity of this module can be captured by measuring the overall connectivity of the actin network. Image segmentation of phalloidin-stained cells was used to skeletonize the actin network architecture (Fig. 6A). The same threshold and segmentation parameters were applied to control and α-actinin-depleted cells. The number of junctions and the length of

connected bundles in the actin network skeletons were significantly lower in α-actinin-depleted cells than control cells confirming the lack of structural connectivity in these cells (Fig. 6B).

The contribution to the global traction force field of tensional forces from transverse arcs and radial fibres was assessed by nano-ablation of subcellular structures positioned on the micropattern symmetry axis, 5 µm away from the curved adhesive edge (Fig. 6C). The magnitude and orientation traction force field in ablated structures was inferred from the hydrogel relaxation on which the cells were plated (Fig. 6C; Movie 4). In control cells, the ablated tensional forces produced by transverse arcs were transmitted perpendicular to the micropattern symmetry axis. By contrast, in α-actinin-depleted cells, the ablated tensional forces aligned with the symmetry axis (Fig. 6C). These results confirm that the crosslinking by α-actinin of the actin network is necessary for the transmission of tensional forces across the lamella in the cell. In absence of α-actinin the various elements of the adhesive front of the cell are not properly interconnected, preventing the proper balance of intracellular forces with respect to extracellular adhesion pattern. Therefore, the structural and mechanical interpretations of the adhesive extracellular environment are defective when the crosslinking of actin filaments is reduced.
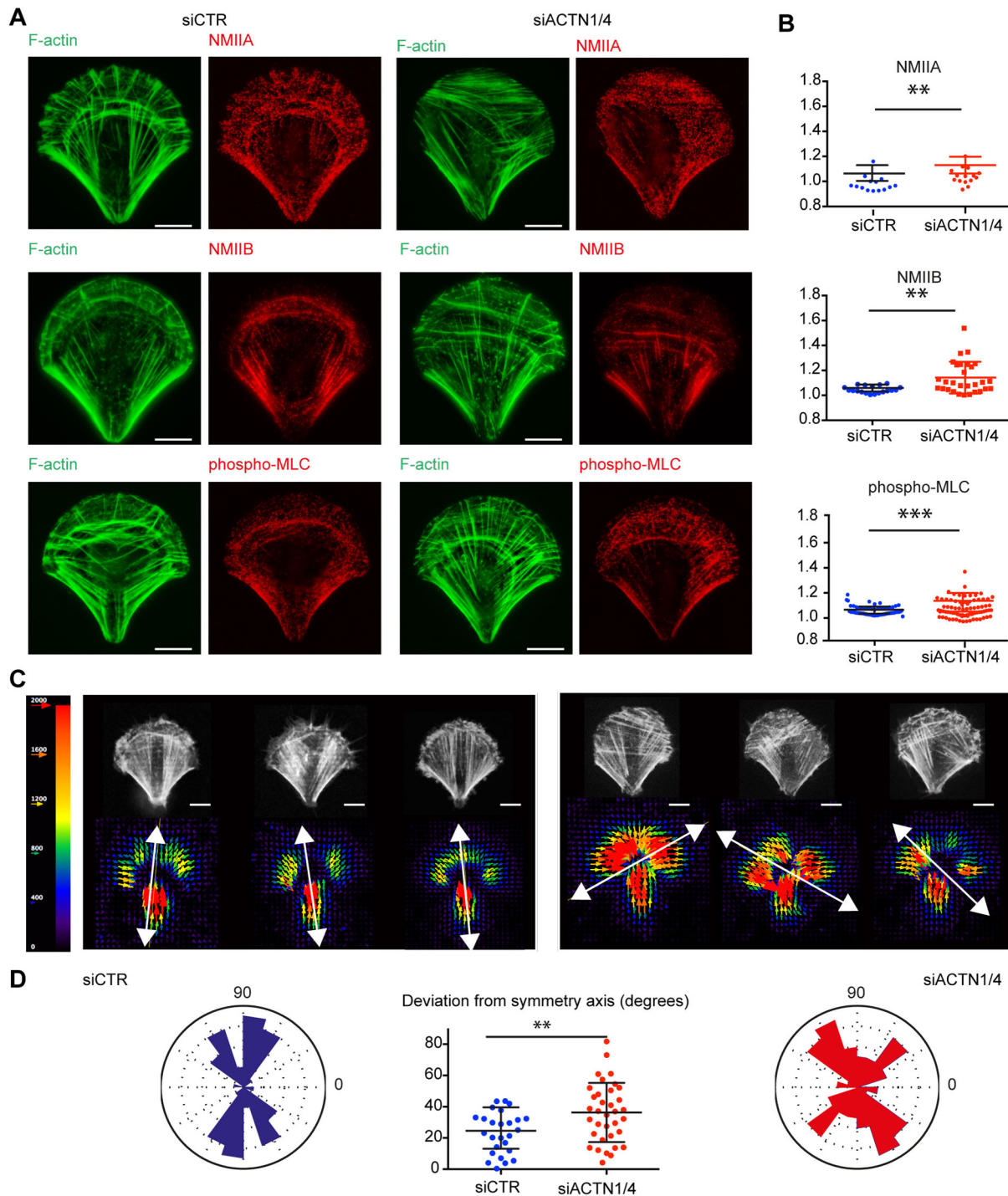
Fig. 5. α-Actinin depletion induces myosin mislocalization and traction force redistribution. (A) F-actin (green) and myosin (red) stainings in control and α-actinin-depleted cells. The top row shows non-muscle myosin IIA (NMIIA), the second row non-muscle myosin IIB (NMIIB) and third row phosphorylated myosin light chains (phospho-MLC). (B) Myosin fluorescence signal intensities were measured in each half of the cell with respect to the micropattern symmetry axis. Graphs show the ratio of the maximal to the minimal intensity. Non-muscle myosin IIA (NMIIA), siCTR, n=14; siACTN1/4=15; non-muscle myosin IIB (NMIIB), siCTR, n=19; siACTN1/4=31; phospho-myosin light chain (phospho-MLC), siCTR, n=63; siACTN1/4=79. **P<0.005 (NMIIA, P=0.0043; NMIIB, P=0.0017); ***P<0.0001 (Mann–Whitney test). (C) Images show traction force fields in control (siCTR; left) and α-actinin-depleted cells (siACTN1/4; right). Arrows indicate force orientation, and colour and length represent local stress magnitude in pascals (Pa). Force dipole calculation revealed the main axis within force field (white double-headed arrow). (D) Rose plot depicting the frequency distribution of the calculated force dipoles orientation for siCTR in blue (n=26) and siACTN1/4 in red (n=35). Graph depicts deviation (in degrees) from symmetry axis. **P=0.0097 (Mann–Whitney test). Scale bars: 10 μm.

Defective integration of spatial cues in α-actinin-depleted cells

Our results showed that α-actinin-depleted cells were defective in the establishment of a balanced actin network architecture with respect to extracellular cues. We further hypothesized that α-actinin-depleted cells are defective in the sensation and adaptation of their architecture in response to local changes in their environment. The absence of large-scale connectivity between different cell parts in α-actinin-
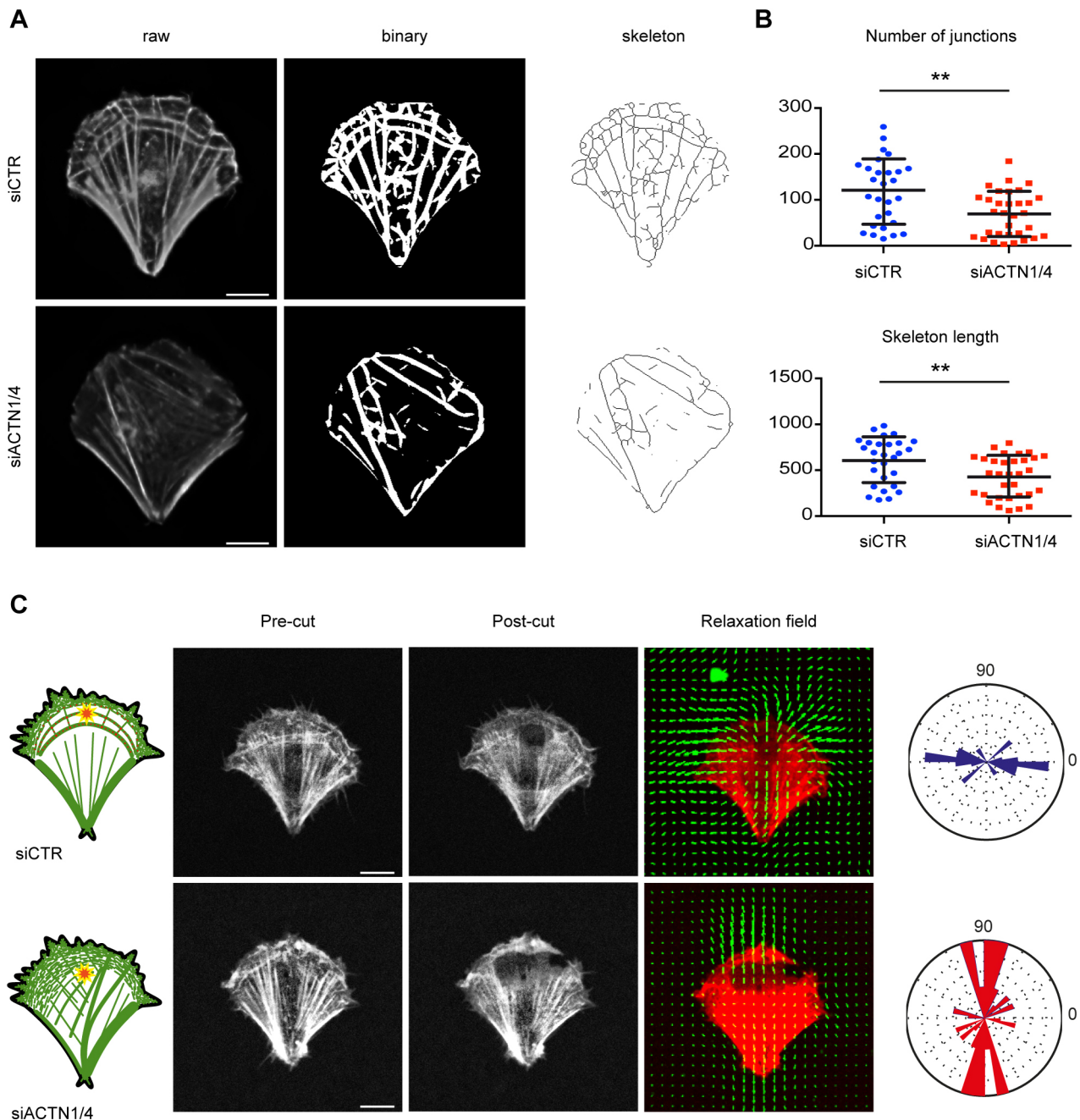
Fig. 6. Lack of actin network connectivity and disruption of transmission of intracellular tension upon α-actinin depletion. (A) Images show F-actin staining in RPE1 cells plated on crossbow-shaped micropatterns (left), filtered, segmented and binarized images (centre), and the corresponding skeletons (right) in control (siCTR; top row) and α-actinin-depleted cells (siACTN1/4; bottom row). (B) The number of junctions between branches were measured on skeletonized images and compared between control and α-actinin-depleted cells. Length of skeleton corresponds to the product of average branch length times number of branches (siCTR, n=28; siACTN1/4, n=32). **P<0.005 (P=0.0042 for junctions, and P=0.0044 for Skeleton length; Mann–Whitney test). (C) RPE1 cells expressing LifeAct–GFP were seeded on crossbow-shaped micropatterns on a compliant substrate. Schemes show the localization of nano-ablated regions on control (siCTR; upper row) and α-actinin-depleted cells (siACTN1/4; bottom row). Images show actin network before (left) and after (centre) nano-ablation. Images on the right show the relaxation of the traction force field upon ablation. Graphs show the angular distribution of the principal direction of the relaxation in control (siCTR, n=15) and α-actinin-depleted (siACTN1/4, n=27) cells. Scale bars: 10 μm.

depleted cells may impair their ability to integrate local changes in their global internal architecture. To examine this hypothesis, we designed an experiment in which the responses of cells were measured following exposure to anisotropic cues in real time.

The anisotropic cues to plated cells were provided by laser-based micropatterning of additional adhesion sites *in situ* and in real time (Vignaud et al., 2012). Two adhesion areas with different distinct distance between adhesion spots were positioned on each side of the symmetry axis (Fig. 7A; Movie 5). The cell outline was monitored for 4 h following the live-patterning of the two distinct adhesive areas (Fig. 7B). In control cells and after 1 h, the protrusions tended to be orientated towards the denser of the two new adhesion sites (Fig. 7C). By contrast, in α-actinin-depleted cells, the protrusions were orientated randomly with respect to the densities of the
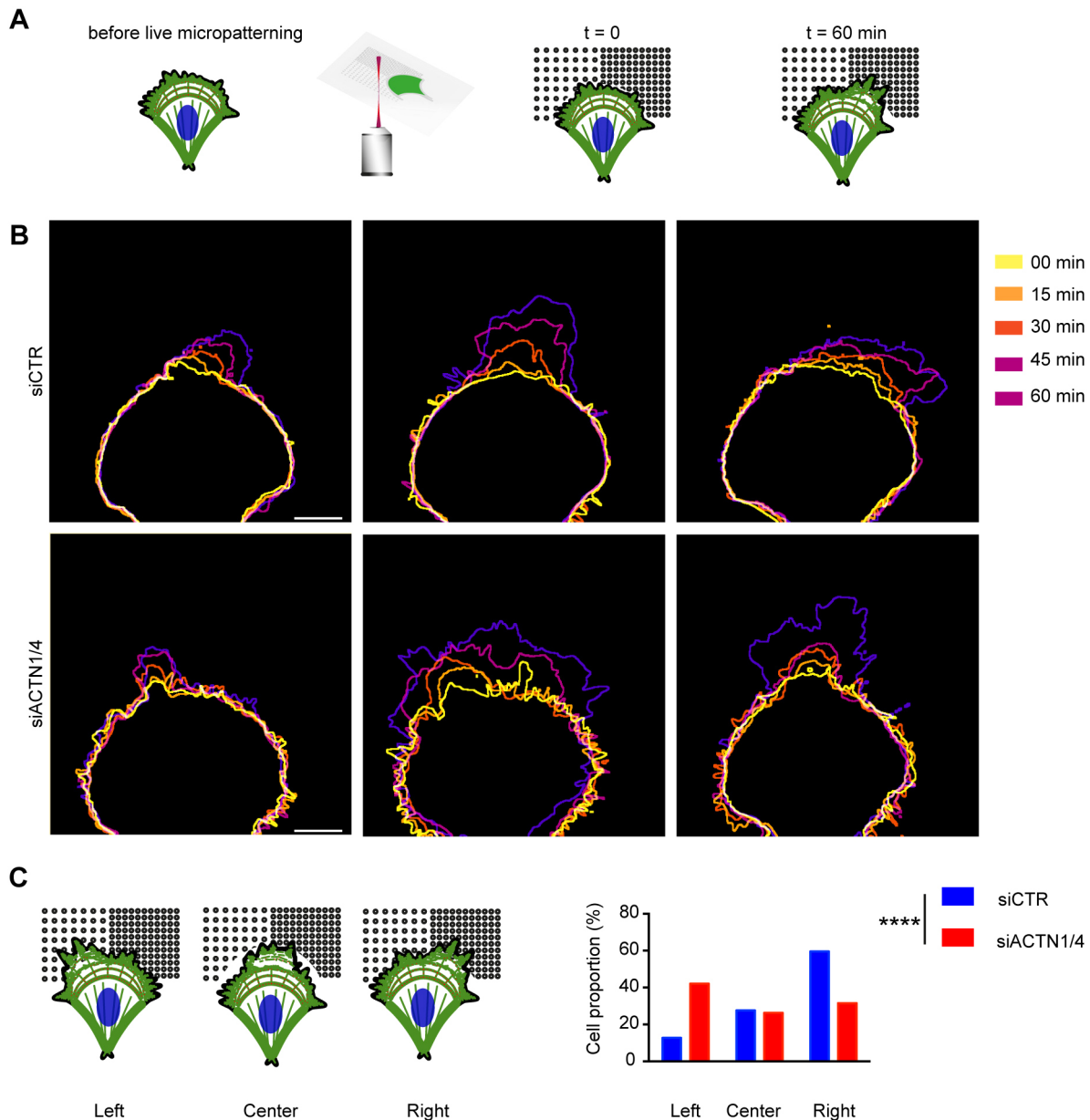
Fig. 7. Defective physical integration of external signals upon α-actinin depletion. (A) RPE1 cells were seeded on a crossbow-shaped micropattern (left). A pulsed UV laser was used to remove the anti-fouling coating next to the live cell (centre). Two adhesive areas of different densities were added in front of the cell plated on the crossbow micropattern. The cell was monitored for 4 h after the addition of the new patterns (right). (B) Images show the contour of control (siCTR; upper row) and α-actinin-depleted cells (siACTN1/4; bottom row) as cells extend over the new micropatterned adhesion sites. (C) Cell shape was scored 1 h after the onset of cell movement. Graphs show the frequency of cell movement toward the left, the centre or the right. Control cells displayed a preferential motion toward the denser adhesive region whereas α-actinin-depleted cells could not distinguish the two (siCTR, n=47; siACTN1/4, n=114). ****P<0.0001 (χ-squared test). Scale bars:10 μm.

adhesion sites (Fig. 7C), suggesting that α-actinin is a necessary part of the adaptation of the cell to the complexities of the extracellular environment through its role in the integration of diverse mechanical signals from that environment. It is also possible that in conjunction with the loss of connectivity, impaired α-actinin function in focal adhesions (Roca-Cusachs et al., 2013; Meacci et al., 2016) contributes to the inability of a α-actinin-depleted cell to distinguish between substrates with different adhesiveness.

DISCUSSION
Our results provide a quantitative description of the remarkable ability of the cell cytoskeleton to self-organize into a contractile architecture that harmonizes with the symmetries and anisotropies of the extracellular environment. The alignment by the retrograde flow of actin filaments into radial fibres attached to cell adhesions, and the interconnections of those fibres, regulate the transmission of intracellular forces in a cell-wide structure, thus resulting in the geometry of the entire cellular architecture being dictated by the spatial distribution of cell adhesions to the extracellular matrix (Fig. 8). Our results were consistent with previous observations (Tee et al., 2015) and confirmed that α-actinin, which ensures the connection of transverse arcs with radial fibres and thereby with cell adhesions, plays a key role in ensuring the correct functioning of this mechanism.
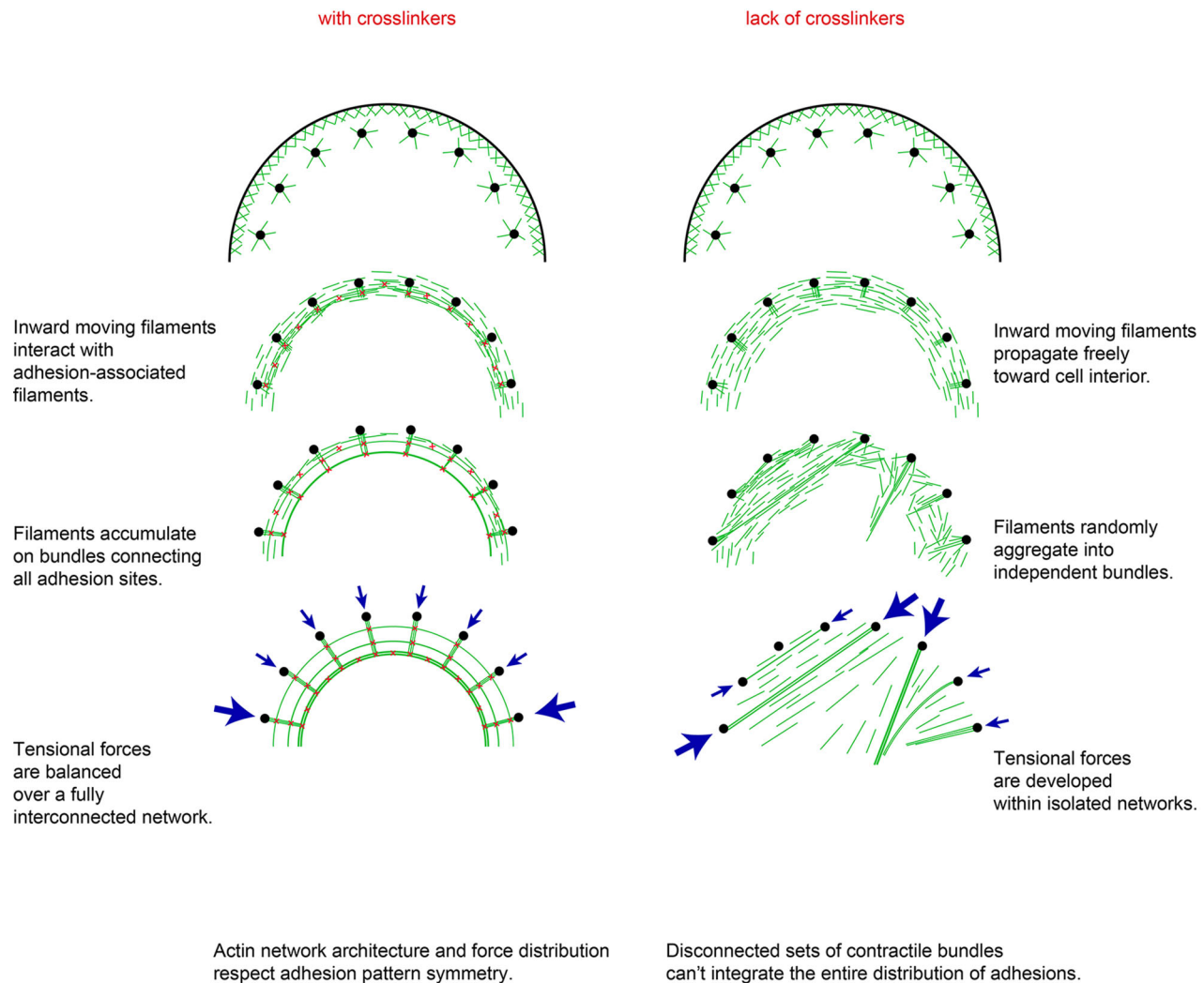
Fig. 8. Actin network dynamics in the cell above the curved adhesive edge in presence or absence of α-actinin. The schemes show the speculative journey of actin filaments from their nucleation (top) to their incorporation into contractile networks (bottom) in control (left) and α-actinin-depleted cells.

As previously described, we found that α-actinin knockdown increases the magnitude of traction forces (Oakes et al., 2012) (Fig. 5C). α-Actinin has numerous binding partners, which is indicative of functions that extend beyond bundling of actin filaments (Otey and Carpen, 2004; Sjöblom et al., 2008). Notably, α-actinin localizes to cell adhesions where it promotes their maturation (Roca-Cusachs et al., 2013; Meacci et al., 2016). In addition, α-actinin modulates actin dynamics and contractility by competing with other actin-binding proteins (Gateva et al., 2017; Kemp and Brieher, 2018). We also found that α-actinin knockdown perturbs the orientation of contractile forces. The two processes may be directly related, since high local forces pull on adjacent filaments; their reorientation contributes to reinforce the local contraction but also perturbs the orientation of the entire network in a mecano-cumulative effect (Luo et al., 2013; Schiffhauer et al., 2016).

The rules describing the physical regulation of cell size and shape are becoming better understood (Paluch and Heisenberg, 2009; Barnhart et al., 2011; Albert and Schwarz, 2014; Marshall, 2015). However, despite a wealth of information about symmetry breaking (Pohl, 2015), the rules describing the establishment of cell symmetry are less clear. Cell symmetry is a signature of how

geometrical and mechanical consistency is maintained within a cell. Marine organisms, which can be considered to be devoid of spatial boundary conditions, display shapes with high levels of symmetry (Sardet, 2015). Recently, jellyfish symmetry has been shown to be dependent on its contractility (Abrams et al., 2015). At the single-cell level, contractility, mediated by myosin II, was shown to prevent cells from fragmenting and to maintain cytoskeletal coherence (Cai et al., 2010). Our results suggest that cytoskeletal coherence also requires actin network crosslinking to ensure that tensional forces are distributed throughout the entire actin network, including cell adhesions. In support of this idea, we have shown elsewhere that the force generated by myosins is not sufficient to support actin network contractility, but that this also requires a precise control of actin network connectivity (Ennomani et al., 2016). Interestingly, α-actinin, unlike other actin filament crosslinkers, is involved in two key functions: network connectivity and cell adhesion maturation (Peterson et al., 2004; Hotulainen and Lappalainen, 2006; Roca-Cusachs et al., 2013). Hence α-actinin could be viewed as a master integrator of the intracellular constraints created by tensional forces, which ensures cytoskeletal coherence and the alignment of the cytoskeletal architecture with the geometry of extracellular adhesive cues.

MATERIALS AND METHODS
In vitro experiments
The detailed procedure can be found elsewhere (Ennomani et al., 2016). In brief, the pWA domain of the Wiskott–Aldrich syndrome protein was adsorbed on the micropatterns and thus promoted actin polymerization upon actin mix addition. The presence of double-headed (heavy meromyosin, HMM) myosin VI was used to induce network contraction (Reymann et al., 2012). The actin mix consisted of 2 µM actin monomers (7% labelled with Alexa Fluor 568), 6 µM profilin, 100 nM Arp2/3 complex and 16 nM of HMM myosin VI (GFP labelled). Proteins were diluted in freshly prepared buffer [15 mM imidazole-HCl pH 7.8, 0.6 mM ATP, 55 mM DTT, 1 mM EGTA, 75 mM KCl, 3.5 mM MgCl$_2$, 1.5 mg/ml glucose, 10 µg/ml catalase, 50 µg/ml glucose oxidase and 0.25% (w/v) methylcellulose]. An ATP-regenerating system was added (2 mM MgATP, 2 mM phosphoenolpyruvate and 2000 U/ml pyruvate kinase). Network contraction was manipulated via the presence (20 nM) or absence of α-actinin 4.

Ring contraction was measured by time-lapse microscopy at one image per minute on an Olympus BX61 microscope with a 40× dry objective (N.A. 0.75), a Marzhauser motorized stage and a CoolSnapHQ2 camera (Roper Scientific). The system was controlled via Metamorph software (Molecular Devices).

Cell lines
Human telomerase-immortalized, retinal-pigmented epithelial cells (RPE1; Clontech) and RPE1 expressing Lifeact–GFP (Vignaud et al., 2012) were grown in a humidified incubator at 37°C and 5% CO$_2$ in DMEM/F12 supplemented with 10% fetal bovine serum and 1% penicillin-streptomycin. All cell culture products were purchased from GIBCO/Life Technologies. Cell lines were regularly checked for mycoplasma contamination (MycoAlert, Lonza); no authentication has been performed.

siRNA treatment
RPE1 cells were transfected with siRNAs (Qiagen) using Lipofectamine RNAi Max transfection reagent (Life Technologies) at a final concentration of 10 nM following the manufacturer's protocol. Strand sequences were: siACTN4, 5′-GCAGCAUCGUGGACUACAATT-3′; and siACTN1, 5′-GCACCAUCAUGGACCAUUAUT-3′. siRNA specificity was assessed by two approaches. First, a redundancy check. For this, we used a second set of siRNAs directed against ACTN1 and ACTN4, respectively (siACTN1/4 – set02). Strand sequences were as follows: siACTN4, 5′-GACACAUAUCG-CAGGGAATT-3′ and siACTN1, 5′-CACCAUGCAUGCCAUGCAATT-3′. siRNA efficiency was quantified by western blotting and morphological characterization after plating on crossbow patterns (Fig. S3). Second, we performed a rescue experiment. Cells were first transfected with siRNA, followed by the transfection of ACTN1–GFP and ACTN4–GFP which are insensitive to the siRNAs. Transfection was performed with X-tremeGENE HP DNA transfection reagent (Sigma-Aldrich) following the manufacturer's guidelines. Next, cells were sorted (FACSMELODY, BD Bioscience) so as to isolate two populations R– (cells which do not harbour the rescue constructs) and R+ (GFP positive). The efficiency of the approach was assessed by western blotting and morphological analysis after plating on crossbow patterns (Fig. S4). For morphological analysis, only cells with consistent α-actinin localization were taken into account in order to avoid over-expression artefacts.

Antibodies and cytoskeletal labelling agents
Primary antibodies were obtained from the following sources and used at the following dilutions: rabbit anti-GAPDH [Santa Cruz Biotechnology, #25778; 1:2000 for western blotting (WB)], rabbit anti-phospho myosin light chain 2 (Ser19) [Cell Signaling Technology #3671; 1:50 for immunofluorescence (IF)], rabbit anti-ACTN1 (Sigma #HPA006035; 1:500 WB, 1:100 IF), mouse anti-ACTN4 (Abcam ab59458; 1:1000 WB, 1:100 IF), rabbit anti-myosin IIa (Cell Signaling Technology #3403; 1:100 for IF), rabbit anti-myosin IIb (Cell Signaling Technology #3404; 1:200 for IF). Alexa Fluor-conjugated phalloidin (Molecular Probes) was resuspended in methanol and diluted 1:500 in PBS for immunostaining. Alexa Fluor-conjugated secondary antibodies (Molecular Probes) were diluted 1:1000.

Immunostaining
Cells were fixed in 4% paraformaldehyde in cytoskeleton buffer pH 6.1 for 15 min at room temperature. They were then washed twice with PBS and incubated in quenching agent (0.1 M ammonium chloride in PBS) for 10 min. Cells were then permeabilized in 0.1% Triton X-100 in PBS for 3 min. For phospho-myosin immunostaining, cells were pre-permeabilized for 15 s with 0.1% Triton X-100 in cytoskeleton buffer prior to paraformaldehyde fixation for 15 min. Paraformaldehyde autofluorescence was quenched by ammonium chloride incubation.

For all conditions, after fixation, the cells were washed, then blocked with 1.5% bovine serum albumin (BSA) for 30 min. The cells were stained with primary antibodies diluted in PBS with 1.5% BSA for 1 h, followed by extensive washing with PBS and staining with secondary antibodies diluted in PBS with 1.5% BSA for 30 min. After washing, the cells were incubated with Alexa Fluor-conjugated phalloidin for 20 min. The cells were washed with PBS and the DNA labelled with 0.2 µg/ml DAPI (Sigma) for 10 min. After washing the cells with water, the coverslips were air-dried and mounted onto slides using Mowiol.

Image acquisition
Images of fixed cells were acquired using either an upright microscope (BX61; Olympus) with 100× (1.4 N.A) oil immersion objective mounted on a piezo ceramic (Physics Instruments), controlled with MetaMorph, or a Leica-TCS-SP2 confocal microscope with a 63× (0.9 N.A) oil immersion objective.

High-resolution images of ACTN4 localization (Fig. S1) were acquired on a Zeiss LSM880 AxioObserver equipped with an Airyscan module, with a Plan-Apochromat 63× (1.4 N.A.) Oil DIC M27 objective. Images were subjected to Airyscan Processing to achieve high resolution.

Western blotting
RPE1 cells were lysed at 4°C in RIPA buffer (Thermo Fisher Scientific) supplemented with 1× protease inhibitor cocktail (Roche). Supernatants were collected and SDS polyacrylamide gel electrophoresis was performed, with samples transferred onto nitrocellulose membrane using a semi-dry western blotting apparatus (BioRad). The membranes were blocked with PBS containing 5% non-fat milk for 1 h at room temperature. After blocking, the membranes were probed with primary antibodies overnight at 4°C. The membranes were washed four times with blocking buffer before adding HRP-conjugated secondary antibodies (Life Technologies), diluted as recommended in blocking buffer, and incubating for 30 min at room temperature. After washing three times with PBS containing 0.1% Tween-20 (Sigma) the membranes were developed using ECL reagent (Life Technologies) and imaged on the ChemiDoc system (BioRad) or by exposing to scientific imaging film (Kodak).

Glass patterning
The detailed procedure is as already described elsewhere (Azioune et al., 2010). In brief, glass coverslips were spin-coated (30 s, 3000 rpm) with adhesion promoter Ti-Prime (MicroChemicals), then cured for 5 min at 120°C and further spin-coated (30 s, 1000 rpm) with 1% polystyrene (Sigma) in toluene (Sigma). Coated coverslips were next oxidized by oxygen plasma (FEMTO, Diener Electronics) (10 s, 30 W) and incubated for 30 min with 0.1 mg/ml poly(L-lysine)-graft-poly(ethylene glycol) (PLL-g-PEG; PLL20K-G35-PEG2K, JenKem) in 10 mM HEPES pH 7.4. Dried coverslips were then exposed to deep-UV (UVO cleaner, Jelight) through a photomask (Toppan) for 4 min. After UV treatment, coverslips were incubated with 10 µg/ml fibronectin (Sigma) and 10 µg/ml Alexa Fluor 546–fibrinogen conjugate (Invitrogen) in PBS for 30 min.

Soft patterning
The detailed procedure is as already described elsewhere (Vignaud et al., 2014). In brief, a quartz photomask was oxidized through oxygenplasma (Femto, Diener Electronics) for 3 min at 100 W before incubation with 0.1 mg/ml PLL-g-PEG in 10 mM HEPES, pH 7.4, for 30 min. After drying, uncoated photomask side was exposed to deep-UV for 5 min. Next, the PLL-PEG-coated side was incubated with 10 µg/ml fibronectin (Sigma) and

10 μg/ml Alexa Fluor 647–fibrinogen conjugate (Invitrogen) in 100 mM sodium bicarbonate buffer, pH 8.4, for 30 min. Acrylamide (8%) and bis-acrylamide solution (0.264%) (Sigma) was degassed for 30 min, mixed with passivated fluorescent beads (Invitrogen) by sonication before addition of ammonium persulfate (APS) and tetramethylethylenediamine (TEMED). 25 μl of that solution was applied on the micropatterned photomask, covered with a silanized coverslip and allow to polymerize for 30 min. Protocols for bead passivation and glass silanization can be found elsewhere (Tseng et al., 2012). The gel was allowed to swell in 100 mM sodium bicarbonate buffer and gently removed. Coverslips were rinsed with PBS before cell plating.

The Young's modulus of the gels was measured to be ∼35 kPa by atomic force microscopy.

Traction force microscopy

Imaging was performed with a confocal spinning disk system consisting of an EclipseTi-E Nikon inverted microscope, equipped with a CSUX1-A1 Yokogawa confocal head, an Evolve EMCCD camera (Roper Scientific, Princeton Instruments) and a Nikon CFI Plan-APO VC 60×, 1.4 N.A. oil immersion objective, interfaced with MetaMorph software (Universal Imaging).

Displacement fields were obtained from bead images before and after removal of cells by trypsin treatment. Bead images were first aligned to correct for experimental drift. The displacement field was calculated by particle image velocimetry (PIV) on the basis of normalized cross-correlation following an iterative scheme. The final grid size was 0.267 μm×0.267 μm. Erroneous vectors were discarded on the basis of a low correlation value and replaced by the median value of the neighbouring vectors. The traction-force field was subsequently reconstructed by Fourier transform traction cytometry, with a regularization parameter set to 2×10^{-10}. Detailed procedures and code are freely available (Martiel et al., 2015).

Force dipole analysis was performed as described previously (Butler et al., 2002; Mandal et al., 2014) using a custom-written MATLAB code.

Laser dissection

UV-laser-based nano-ablation was performed on the spinning disk system using the iLas2 device (Roper Scientific, France). iLas2 is a dual axis galvanometer-based optical scanner that focuses the laser beam on the sample. The system includes a telescope to adjust laser focus and a motorized polarizer to control beam power. We used a passively Q-switched laser (STV-E, TeamPhotonics, France) producing 300 ps pulses at 355 nm. Laser displacement, exposure time and repetition rate were controlled via ILas software interfaced with MetaMorph (Universal Imaging Corporation). Laser ablation and subsequent imaging was performed with a 100× CFI S Fluor oil objective (MRH02900, Nikon). The ablation region was exposed for 12 ms at a repetition rate of 7000 Hz. Pulse energy was set to 300 nJ before objective by adjusting the polarizer.

Live laser patterning

RPE1–Lifeact–GFP cells were seeded on patterned coverslips without prior protein coating and allowed to attach for 3 h. Live laser patterning was performed as described previously (Vignaud et al., 2012). In brief, patterning was performed on the aforementioned spinning disk system (see section on traction force microscopy), combined with iLas2 (Roper Scientific, France) and a 100× CFI S Fluor oil objective (MRH02900, Nikon). We used a passively Q-switched laser with a 355 nm wavelength. Patterns were designed in Illustrator (Adobe) and imported into iLas software. Typical patterns consist of arrays of 1 μm diameter spots, with a pitch of 3 μm (high spot density) or 4 μm (low spot density).

Transverse arcs tracking

RPE1–Lifeact–GFP cells were seeded on patterned coverslips and allowed to spread for 3 h. Time-lapse images were acquired on spinning disk system with a Nikon CFI PlanApo 60× oil objective (N.A. 1.4). Over a period of 20 min, we acquired, every minute, a z-stack consisting of five planes covering 5 μm of the basal plane of the cell. Illumination was set so as to have highest dynamical range at the leading edge of the cell. Resulting stacks were analysed with the 'Analyze Tubeness' function bundled with the freely available FIJI software (https://fiji.sc/). Particle image velocimetry (see section on traction force microscopy) was performed on the maximum projection of each stack with the

freely available software PIVLab (Thielicke and Stamhuis, 2014). PIVlab was employed by performing a double cross correlation analysis, with an interrogation area of 30 pixels with a step of 15 pixels. We produced average flow fields giving access to mean flow speed and orientation.

Image analysis
Directionality

Each cell was divided in two equal regions of interest (ROI) following the patterns symmetry axis. Actin fibre orientation was assessed with two freely available ImageJ plugins (https://imagej.nih.gov/ij/): Directionality, as implemented by J-Y Tinevez (http://imagej.net/Directionality), and OrientationJ, as implemented by D. Sage (http://bigwww.epfl.ch/demo/orientation/). Orientation distributions were compared with a Kolmogorov–Smirnov test, where D is the difference between fibre orientation distribution between each part of the cell. Both approaches gave similar results.

Fluorescence measurement

Myosin IIA, IIB and pMLC signals were analysed with ImageJ (https://imagej.nih.gov/ij/). Each cell was divided in two equal ROIs, following the pattern symmetry axis. Fluorescence intensity was measured in each ROI. The ratio of fluorescence intensity between each region of interest describes to what extent the signal distribution is symmetric with respect to the pattern symmetry axis.

Connectivity analysis

The actin cytoskeleton was segmented following two strategies based on ridge detection. The first approach was based on ridge detection with SteerableJ an ImageJ plugin implemented by François Aguet (http://bigwww.epfl.ch/demo/steerable/download.html) (Jacob and Unser, 2004) and the second approach used Ridge_Detection as implemented by Wagner and Hiner (http://imagej.net/Ridge_Detection) (Steger, 1998). Both approaches produced similar structures. Next, the binary image was skeletonized and analysed using ImageJ. The ImageJ function 'Analyze skeleton' allowed the extraction of the number of connections and the skeleton length from the skeletonized image. Skeleton length refers to the biggest skeleton in the considered cell and is the product between number of branches and average branch length as given by the ImageJ function 'Analyze skeleton'.

Nucleus positioning

DAPI-stained nuclei were first LoG filtered. LoG filter consists of two steps. First, a Gaussian filter is applied to smooth the image. Then a Laplacian filter is used to enhance the edges. Images were thresholded with an automatic Otsu approach, as implemented in ImageJ (https://imagej.net/Auto_Threshold#Otsu), and segmented. Image processing was performed in ImageJ. Nuclei coordinates were approximated to the centre of mass of the segmented nucleus. These coordinates were measured relatively to the geometric centre of the micropattern.

Statistical analysis

Statistical analysis was performed with Graphpad Prism, version 07. Data from at least three independent experiments are expressed as mean±s.d. All data, except for live laser patterning (Fig. 7), was analysed with a two-tailed Mann–Witney test. For live patterning and cell migration (Fig. 7), data were analysed with a Chi-square test.

Competing interests
The authors declare no competing or financial interests.

Author contributions
Conceptualization: L.B., M.T.; Methodology: F.S., H.E., L.K., M.T.; Software: L.K.; Validation: L.K.; Formal analysis: H.E., L.K., M.T.; Investigation: F.S., A.P., H.E., L.K.; Resources: A.P.; Data curation: F.S., H.E., L.K.; Writing - original draft: F.S.,

M.T.; Writing - review & editing: F.S., M.T.; Supervision: L.B., M.T.; Project administration: L.B., M.T.; Funding acquisition: L.B., M.T.

References
Abrams, M. J., Basinger, T., Yuan, W., Guo, C.-L. and Goentoro, L. (2015). Self-repairing symmetry in jellyfish through mechanically driven reorganization. *Proc. Natl. Acad. Sci. USA* **112**, E3365-E3373. doi:10.1073/pnas.1502497112

Abu Shah, E. and Keren, K. (2014). Symmetry breaking in reconstituted actin cortices. *eLife* **3**, 1-15. doi:10.7554/eLife.01433

Albert, P. J. and Schwarz, U. S. (2014). Dynamics of cell shape and forces on micropatterned substrates predicted by a cellular Potts model. *Biophys. J.* **106**, 2340-2352. doi:10.1016/j.bpj.2014.04.036

Azioune, A., Carpi, N., Tseng, Q., Théry, M. and Piel, M. (2010). Protein micropatterns: a direct printing protocol using deep UVs. *Methods Cell Biol.* **97**, 133-146. doi:10.1016/S0091-679X(10)97008-8

Barnhart, E. L., Lee, K.-C., Keren, K., Mogilner, A. and Theriot, J. A. (2011). An adhesion-dependent switch between mechanisms that determine motile cell shape. *PLoS Biol.* **9**, e1001059. doi:10.1371/journal.pbio.1001059

Belmonte, J. M., Leptin, M. and Nédélec, F. (2017). A theory that predicts behaviors of disordered cytoskeletal networks. *Mol. Syst. Biol.* **13**, 941. doi:10.15252/msb.20177796

Blanchoin, L., Boujemaa-Paterski, R., Sykes, C. and Plastino, J. (2014). Actin dynamics, architecture, and mechanics in cell motility. *Physiol. Rev.* **94**, 235-263. doi:10.1152/physrev.00018.2013

Burnette, D. T., Manley, S., Sengupta, P., Sougrat, R., Davidson, M. W., Kachar, B. and Lippincott-schwartz, J. (2011). A role for actin arcs in the leading-edge advance of migrating cells. *Nat. Cell Biol.* **13**, 371-382. doi:10.1038/ncb2205

Butler, J. P., Tolić-Nørrelykke, I. M., Fabry, B. and Fredberg, J. J. (2002). Traction fields, moments, and strain energy that cells exert on their surroundings. *Am. J. Physiol. Cell Physiol.* **282**, C595-C605. doi:10.1152/ajpcell.00270.2001

Cai, Y., Rossier, O., Gauthier, N. C., Biais, N., Fardin, M.-A., Zhang, X., Miller, L. W., Ladoux, B., Cornish, V. W. and Sheetz, M. P. (2010). Cytoskeletal coherence requires myosin-IIA contractility. *J. Cell Sci.* **123**, 413-423. doi:10.1242/jcs.058297

Ciobanasu, C., Faivre, B. and Le Clainche, C. (2014). Actomyosin-dependent formation of the mechanosensitive talin-vinculin complex reinforces actin anchoring. *Nat. Commun.* **5**, 3095. doi:10.1038/ncomms4095

Ennomani, H., Letort, G., Guérin, C., Martiel, J.-L., Cao, W., Nédélec, F., De La Cruz, E. M., Théry, M. and Blanchoin, L. (2016). Architecture and connectivity govern actin network contractility. *Curr. Biol.* **26**, 616-626. doi:10.1016/j.cub.2015.12.069

Gateva, G., Kremneva, E., Reindl, T., Kotila, T., Kogan, K., Gressin, L., Gunning, P. W., Manstein, D. J., Michelot, A. and Lappalainen, P. (2017). Tropomyosin isoforms specify functionally distinct actin filament populations in vitro. *Curr. Biol.* **27**, 705-713. doi:10.1016/j.cub.2017.01.018

Gomes, E. R., Jani, S. and Gundersen, G. G. (2005). Nuclear movement regulated by Cdc42, MRCK, myosin, and actin flow establishes MTOC polarization in migrating cells. *Cell* **121**, 451-463. doi:10.1016/j.cell.2005.02.022

Hotulainen, P. and Lappalainen, P. (2006). Stress fibers are generated by two distinct actin assembly mechanisms in motile cells. *J. Cell Biol.* **173**, 383-394. doi:10.1083/jcb.200511093

Jacob, M. and Unser, M. (2004). Design of steerable filters for feature detection using Canny-like criteria. *IEEE Trans. Pattern Anal. Mach. Intell.* **26**, 1007-1019. doi:10.1109/TPAMI.2004.44

Jensen, M. H., Morris, E. J. and Weitz, D. A. (2015). Mechanics and dynamics of reconstituted cytoskeletal systems. *Biochim. Biophys. Acta Mol. Cell Res.* **1853**, 3038-3042. doi:10.1016/j.bbamcr.2015.06.013

Jiu, Y., Lehtimäki, J., Tojkander, S., Cheng, F., Jäälinoja, H., Liu, X., Varjosalo, M., Eriksson, J. E. and Lappalainen, P. (2015). Bidirectional interplay between Vimentin intermediate filaments and contractile actin stress fibers. *Cell Rep.* **11**, 1511-1518. doi:10.1016/j.celrep.2015.05.008

Kemp, J. P. and Brieher, W. M. (2018). The actin filament bundling protein α-actinin-4 actually suppresses actin stress fibers by permitting actin turnover. *J. Biol. Chem.* **293**, 14520-14533. doi:10.1074/jbc.RA118.004345

Kovac, B., Teo, J. L., Mäkelä, T. P. and Vallenius, T. (2013). Assembly of non-contractile dorsal stress fibers requires α-actinin-1 and Rac1 in migrating and spreading cells. *J. Cell Sci.* **126**, 263-273. doi:10.1242/jcs.115063

Letort, G., Ennomani, H., Gressin, L., Théry, M. and Blanchoin, L. (2015). Dynamic reorganization of the actin cytoskeleton. *F1000 Res.* **4**, 940. doi:10.12688/f1000research.6374.1

Levayer, R. and Lecuit, T. (2012). Biomechanical regulation of contractility: spatial control and dynamics. *Trends Cell Biol.* **22**, 61-81. doi:10.1016/j.tcb.2011.10.001

Linsmeier, I., Banerjee, S., Oakes, P. W., Jung, W., Kim, T. and Murrell, M. P. (2016). Disordered actomyosin networks are sufficient to produce cooperative and telescopic contractility. *Nat. Commun.* **7**, 12615. doi:10.1038/ncomms12615

Luo, T., Mohan, K., Iglesias, P. A. and Robinson, D. N. (2013). Molecular mechanisms of cellular mechanosensing. *Nat. Mater.* **12**, 1064-1071. doi:10.1038/nmat3772

Mak, M., Zaman, M. H., Kamm, R. D. and Kim, T. (2016). Interplay of active processes modulates tension and drives phase transition in self-renewing, motor-driven cytoskeletal networks. *Nat. Commun.* **7**, 10323. doi:10.1038/ncomms10323

Mandal, K., Wang, I., Vitiello, E., Orellana, L. A. C. and Balland, M. (2014). Cell dipole behaviour revealed by ECM sub-cellular geometry. *Nat. Commun.* **5**, 5749. doi:10.1038/ncomms6749

Marshall, W. F. (2015). Cell geometry: how cells count and measure size. *Annu. Rev. Biophys.* **45**, 49-64. doi:10.1146/annurev-biophys-062215-010905

Martiel, J.-L., Leal, A., Kurzawa, L., Balland, M., Wang, I., Vignaud, T., Tseng, Q. and Théry, M. (2015). Measurement of cell traction forces with ImageJ. *Methods Cell Biol.* **125**, 269-287. doi:10.1016/bs.mcb.2014.10.008

Meacci, G., Wolfenson, H., Liu, S., Stachowiak, M. R., Iskratsch, T., Mathur, A., Ghassemi, S., Gauthier, N., Tabdanov, E., Lohner, J. et al. (2016). α-actinin links ECM rigidity sensing contractile units with periodic cell edge retractions. *Mol. Biol. Cell.* **27**, 3377-3685. doi:10.1091/mbc.e16-02-0107

Murrell, M. P. and Gardel, M. L. (2012). F-actin buckling coordinates contractility and severing in a biomimetic actomyosin cortex. *Proc. Natl. Acad. Sci. USA* **109**, 20820-20825. doi:10.1073/pnas.1214753109

Naumanen, P., Lappalainen, P. and Hotulainen, P. (2008). Mechanisms of actin stress fibre assembly. *J. Microsc.* **231**, 446-454. doi:10.1111/j.1365-2818.2008.02057.x

Oakes, P. W., Beckham, Y., Stricker, J. and Gardel, M. L. (2012). Tension is required but not sufficient for focal adhesion maturation without a stress fiber template. *J. Cell Biol.* **196**, 363-374. doi:10.1083/jcb.201107042

Otey, C. A. and Carpen, O. (2004). Alpha-actinin revisited: a fresh look at an old player. *Cell Motil. Cytoskeleton* **58**, 104-111. doi:10.1002/cm.20007

Paluch, E. and Heisenberg, C.-P. (2009). Biology and physics of cell shape changes in development. *Curr. Biol.* **19**, R790-R799. doi:10.1016/j.cub.2009.07.029

Peterson, L. J., Rajfur, Z., Maddox, A. S., Freel, C. D., Chen, Y., Edlund, M., Otey, C. and Burridge, K. (2004). Simultaneous stretching and contraction of stress fibers in vivo. *Mol. Biol. Cell* **15**, 3497-3508. doi:10.1091/mbc.e03-09-0696

Pohl, C. (2015). Cytoskeletal symmetry breaking and chirality: from reconstituted systems to animal development. *Symmetry (Basel)* **7**, 2062-2107. doi:10.3390/sym7042062

Quick, Q. and Skalli, O. (2010). α-Actinin 1 and α-actinin 4: Contrasting roles in the survival, motility, and RhoA signaling of astrocytoma cells. *Exp. Cell Res.* **316**, 1137-1147. doi:10.1016/j.yexcr.2010.02.011

Reymann, A.-C., Martiel, J.-L., Cambier, T., Blanchoin, L., Boujemaa-Paterski, R. and Théry, M. (2010). Nucleation geometry governs ordered actin networks structures. *Nat. Mater.* **9**, 827-832. doi:10.1038/nmat2855

Reymann, A.-C., Boujemaa-Paterski, R., Martiel, J.-L., Guérin, C., Cao, W., Chin, H. F., De La Cruz, E. M., Théry, M. and Blanchoin, L. (2012). Actin network architecture can determine myosin motor activity. *Science* **336**, 1310-1314. doi:10.1126/science.1221708

Roca-Cusachs, P., Del Rio, A., Puklin-Faucher, E., Gauthier, N. C., Biais, N. and Sheetz, M. P. (2013). Integrin-dependent force transmission to the extracellular matrix by α-actinin triggers adhesion maturation. *Proc. Natl. Acad. Sci. USA* **110**, E1361-E1370. doi:10.1073/pnas.1220723110

Sardet, C. (2015). *Plankton, Wonders of the Drifting World*. Chicago: The Univeristy of Chicago Press.

Schiffhauer, E. S., Luo, T., Mohan, K., Griffis, E. R., Iglesias, P. A., Correspondence, D. N. R., Srivastava, V., Qian, X. and Robinson, D. N. (2016). Mechanoaccumulative elements of the mammalian actin cytoskeleton. *Curr. Biol.* **26**, 1473-1479. doi:10.1016/j.cub.2016.04.007

Schiller, H. B., Hermann, M.-R., Polleux, J., Vignaud, T., Zanivan, S., Friedel, C. C., Sun, Z., Raducanu, A., Gottschalk, K.-E., Théry, M. et al. (2013). β1- and αv-class integrins cooperate to regulate myosin II during rigidity sensing of fibronectin-based microenvironments. *Nat. Cell Biol.* **15**, 625-636. doi:10.1038/ncb2747

Schupplel, M., Keber, F. C., Kröger, M. and Bausch, A. R. (2016). Boundaries steer the contraction of active gels. *Nat. Commun.* **7**, 13120. doi:10.1038/ncomms13120

Shemesh, T., Verkhovsky, A. B., Svitkina, T. M., Bershadsky, A. D. and Kozlov, M. M. (2009). Role of focal adhesions and mechanical stresses in the formation and progression of the lamellum interface. *Biophys. J.* **97**, 1254-1264. doi:10.1016/j.bpj.2009.05.065

Sjöblom, B., Salmazo, A. and Djinović-Carugo, K. (2008). Alpha-actinin structure and regulation. *Cell. Mol. Life Sci.* **65**, 2688-2701. doi:10.1007/s00018-008-8080-8

Steger, G. (1998). An unbiased detector of curvilinear structures. *IEEE Trans. Pattern Anal. Mach. Intell.* **20**, 113-125. doi:10.1109/34.659930

Sun, Z., Tseng, H.-Y., Tan, S., Senger, F., Kurzawa, L., Dedden, D., Mizuno, N., Wasik, A. A., Théry, M., Dunn, A. R. et al. (2016). Kank2 activates talin, reduces force transduction across integrins and induces central adhesion formation. *Nat. Cell Biol.* **18**, 941-953. doi:10.1038/ncb3402

Tee, Y. H., Shemesh, T., Thiagarajan, V., Hariadi, R. F., Anderson, K. L., Page, C., Volkmann, N., Hanein, D., Sivaramakrishnan, S., Kozlov, M. M. et al. (2015). Cellular chirality arising from the self-organization of the actin cytoskeleton. *Nat. Cell Biol.* **17**, 445-457. doi:10.1038/ncb3137

Théry, M. (2010). Micropatterning as a tool to decipher cell morphogenesis and functions. *J. Cell Sci.* **123**, 4201-4213. doi:10.1242/jcs.075150

Théry, M., Racine, V., Piel, M., Pépin, A., Dimitrov, A., Chen, Y., Sibarita, J.-B. and Bornens, M. (2006). Anisotropy of cell adhesive microenvironment governs cell internal organization and orientation of polarity. *Proc. Natl. Acad. Sci. USA* **103**, 19771-19776. doi:10.1073/pnas.0609267103

Thielicke, W. and Stamhuis, E. J. (2014). PIVlab – towards user-friendly, affordable and accurate digital particle image velocimetry in MATLAB. *J. Open Res. Softw.* **2**, e30. doi:10.5334/jors.bl

Tojkander, S., Gateva, G. and Lappalainen, P. (2012). Actin stress fibers - assembly, dynamics and biological roles. *J. Cell Sci.* **125**, 1855-1864. doi:10.1242/jcs.098087

Tojkander, S., Gateva, G., Husain, A., Krishnan, R. and Lappalainen, P. (2015). Generation of contractile actomyosin bundles depends on mechanosensitive actin filament assembly and disassembly. *eLife* **4**, e06126. doi:10.7554/eLife.06126

Tseng, Q., Wang, I., Duchemin-Pelletier, E., Azioune, A., Carpi, N., Gao, J., Filhol, O., Piel, M., Théry, M. and Balland, M. (2011). A new micropatterning method of soft substrates reveals that different tumorigenic signals can promote or reduce cell contraction levels. *Lab. Chip* **11**, 2231-2240. doi:10.1039/c0lc00641f

Tseng, Q., Duchemin-Pelletier, E., Deshiere, A., Balland, M., Guillou, H., Filhol, O. and Théry, M. (2012). Spatial organization of the extracellular matrix regulates cell-cell junction positioning. *Proc. Natl. Acad. Sci. USA* **109**, 1506-1511. doi:10.1073/pnas.1106377109

Vignaud, T., Galland, R., Tseng, Q., Blanchoin, L., Colombelli, J. and Théry, M. (2012). Reprogramming cell shape with laser nano-patterning. *J. Cell Sci.* **125**, 2134-2140. doi:10.1242/jcs.104901

Vignaud, T., Ennomani, H. and Théry, M. (2014). Polyacrylamide hydrogel micropatterning. *Methods Cell Biol.* **120**, 93-116. doi:10.1016/B978-0-12-417136-7.00006-9

Vogel, S. K., Petrasek, Z., Heinemann, F. and Schwille, P. (2013). Myosin motors fragment and compact membrane-bound actin filaments. *eLife* **2**, 1-18. doi:10.7554/eLife.00116